SQUID–SIMS is a useful approach to uncover primary signals in the Archean sulfur cycle

Woodward W. Fischer[a,1], David A. Fike[b], Jena E. Johnson[a], Timothy D. Raub[a,c], Yunbin Guan[a], Joseph L. Kirschvink[a], and John M. Eiler[a]

[a]Division of Geological and Planetary Sciences, California Institute of Technology, Pasadena, CA 91125; [b]Department of Earth and Planetary Sciences, Washington University, St. Louis, MO 63130; and [c]Department of Earth Sciences, University of St. Andrews, St. Andrews KY16 9AL, United Kingdom

Edited by Mark H. Thiemens, University of California, San Diego, La Jolla, CA, and approved March 10, 2014 (received for review December 4, 2013)

Many aspects of Earth's early sulfur cycle, from the origin of mass-anomalous fractionations to the degree of biological participation, remain poorly understood—in part due to complications from postdepositional diagenetic and metamorphic processes. Using a combination of scanning high-resolution magnetic superconducting quantum interference device (SQUID) microscopy and secondary ion mass spectrometry (SIMS) of sulfur isotopes (^{32}S, ^{33}S, and ^{34}S), we examined drill core samples from slope and basinal environments adjacent to a major Late Archean (∼2.6–2.5 Ga) marine carbonate platform from South Africa. Coupled with petrography, these techniques can untangle the complex history of mineralization in samples containing diverse sulfur-bearing phases. We focused on pyrite nodules, precipitated in shallow sediments. These textures record systematic spatial differences in both mass-dependent and mass-anomalous sulfur-isotopic composition over length scales of even a few hundred microns. Petrography and magnetic imaging demonstrate that mass-anomalous fractionations were acquired before burial and compaction, but also show evidence of postdepositional alteration 500 million y after deposition. Using magnetic imaging to screen for primary phases, we observed large spatial gradients in Δ^{33}S (>4‰) in nodules, pointing to substantial environmental heterogeneity and dynamic mixing of sulfur pools on geologically rapid timescales. In other nodules, large systematic radial δ^{34}S gradients (>20‰) were observed, from low values near their centers increasing to high values near their rims. These fractionations support hypotheses that microbial sulfate reduction was an important metabolism in organic-rich Archean environments—even in an Archean ocean basin dominated by iron chemistry.

mass independent fractionation | MIF | metamorphism | metasomatism

Patterns emerging from multiple sulfur-isotope ratios in sedimentary rocks have provided powerful insights into the behavior of the Archean (>2.5 Ga) sulfur cycle and the timing of the rise of atmospheric oxygen (1). Sulfur-isotope data from Archean sedimentary successions show distinct differences from those contained in younger successions—in rocks older than ∼2.32 Ga, S-bearing minerals display large deviations in isotope ratios from predicted mass-fractionation relationships, captured by the statistic $\Delta^{33}S$ [$\Delta^{33}S = 1000(\ln(1+(\delta^{33}S/1000)) - 0.515(\ln(1+(\delta^{34}S/1000))$, with $\delta^{34}S = ([^{34}S/^{32}S_{samp}]/[^{34}S/^{32}S_{std}]) - 1)1000$; $\delta^{33}S = ([^{33}S/^{32}S_{samp}]/[^{33}S/^{32}S_{std}]) - 1)1000$; $\Delta^{33}S = 1000(\ln(1+(\delta^{33}S/1000)) - 0.515(\ln(1+(\delta^{34}S/1000))$] and here termed mass-anomalous fractionations (MAF; refs. 1–3). The origin of Archean sulfur-isotope MAF remains imperfectly understood, although most hypotheses implicate atmospheric photochemistry involving SO_2 (1, 4, 5). If this interpretation is correct, photochemical and geochemical models can use stratigraphic sulfur-isotope data to provide quantitative constraints on the oxidative power of the Archean atmosphere (e.g., O_2 mixing ratio $<< 10^{-5}$; ref. 6), continental crust growth, volatile fluxes from the solid earth (7), seawater chemistry, and the degree of biological cycling (8).

In addition to the nature of the MAF that is so conspicuous in Archean strata, questions remain about what role, if any, biology played in the early sulfur cycle. Comparative molecular biology suggests that both sulfide-based photosynthesis and dissimilatory sulfate reduction (DSR) were important early autotrophic and heterotrophic metabolisms, respectively (9, 10). Similar interpretations about DSR have been garnered from modest but notable sulfur-isotope fractionations in Archean samples (11–13). These proxies rely on the premise that differences between isotope ratios captured in sedimentary S-bearing materials can be definitively linked to specific S metabolisms via their expected kinetic isotope fractionations. In general, however, $\delta^{34}S$ variations in Archean pyrites are much smaller than observed in Proterozoic and Phanerozoic rocks, and have average values close to bulk silicate earth (∼0‰; ref. 14). This pattern has plausible end-member interpretations that range from no biological cycling (8, 14) to some biological cycling but with little induced fractionation during DSR due to low seawater sulfate concentrations (< 200 μM; ref. 15), high temperatures (16), or high electron donor concentrations (e.g., ref. 17). An exclusive test of these ideas is challenged by a mass-balance circumstance unique to the Archean sedimentary record—sulfate minerals are exceedingly rare. Early Archean barite deposits like those known from the Dresser Formation of Western Australia (1, 18) and chert-rich successions of similar age in the Barberton Greenstone Belt of South Africa

Significance

A challenge to understanding ancient sulfur-cycle processes on early Earth is the persistent observation that postdepositional processes have affected all Archean-age rocks, impacting geochemical signals, and the quality of paleoenvironmental interpretations. To solve this problem we developed a combination of texture-specific microscale techniques—scanning high-resolution low-temperature superconducting quantum interference device microscopy and secondary ion mass spectrometry. We applied these techniques in a well-studied Archean-age sedimentary succession in South Africa to unravel the mineralization and isotopic history and reveal primary sulfur-cycle processes. We observed systematic patterns of isotope ratios at microscopic scales that inform the nature of enigmatic sulfur-isotope mass anomalies unique to this time interval and further support hypotheses for the early evolution of sulfate-reduction metabolisms.

Author contributions: W.W.F., D.A.F., T.D.R., J.L.K., and J.M.E. designed research; W.W.F., D.A.F., J.E.J., and T.D.R. performed research; W.W.F., D.A.F., J.E.J., T.D.R., Y.G., J.L.K., and J.M.E. contributed new reagents/analytic tools; W.W.F., D.A.F., J.E.J., T.D.R., Y.G., and J.M.E. analyzed data; and W.W.F., D.A.F., and J.E.J. wrote the paper.

The authors declare no conflict of interest.

This article is a PNAS Direct Submission.

Freely available online through the PNAS open access option.

[1]To whom correspondence should be addressed. E-mail: wfischer@caltech.edu.

This article contains supporting information online at www.pnas.org/lookup/suppl/doi:10.1073/pnas.1322577111/-/DCSupplemental.

(19) are uncommon and absent from younger, better-preserved Archean settings. Sulfate minerals are absent from evaporite sequences (20), only becoming a noticeable component of the geological record well after the rise of oxygen (21, 22). These observations confirm that seawater sulfate concentrations were much lower than today, but moreover this creates a fundamental challenge for isotope studies because the primary geochemical sink for sulfur in Archean oceans was in sedimentary pyrite. Given that nearly all Archean seawater sulfur leaves as sedimentary pyrite, the general lack of $\delta^{34}S$ fractionation is expected: regardless of isotopic fractionations during sulfur cycling and pyrite formation, a (nearly) quantitative sink will have an isotopic composition (nearly) identical to the source (16).

The one-sink Archean sulfur cycle is currently underdetermined and it is not straightforward to use sulfur-isotope data to distinguish between a spectrum of sulfur-cycle processes. To test the interpretation that variability of $\delta^{34}S$ values within a sample or paleoenvironment is the result of DSR (11–13), we require a means to observe the isotopic composition of an environmental sulfur reservoir as it evolved along a known reaction path. Here we target pyrite nodules that grew in the sediments during early diagenesis to track the isotopic evolution of the fluid composition as a function of their radius and provide a targeted view into the microbial physiology once present in this environment.

Another and equally critical challenge to interpreting sulfur-isotope ratio data in Archean rocks is the persistent observation that the petrographic textures of sulfide-bearing minerals present in any given rock sample demonstrate complex origins that combine detrital, diagenetic, and metamorphic components. Indeed, a substantially different hypothesis was proposed wherein MAF arises during high-temperature diagenetic reactions involving the interaction of sulfur-bearing fluids with kerogen in the protolith (23, 24). Although this mechanism does not appear to explain the aforementioned secular MAF trends (25), it is important to note that all Archean successions have undergone diagenetic and, in most cases, metasomatic episodes of sulfur mineralization, which complicates interpretation of isotope records (e.g., ref. 26). To test these hypotheses and better capture the nature of MAF signals, we require a better understanding of how sedimentary successions preserve isotopic signatures through complex and protracted histories of sulfur mineralization. Secondary ion mass spectrometry (SIMS) has emerged as a powerful technique for measuring the sulfur-isotope compositions of Archean and Paleoproterozoic rocks, and this approach has demonstrated systematic isotopic differences tied to different pyrite textures (e.g., refs. 13 and 27–29). Here we build on this work using a combination of petrography and microscale magnetic imaging coupled to texture-specific sulfur-isotope measurements using SIMS to evaluate the effects of postdepositional mineralization and better constrain primary paleoenvironmental processes.

We studied a well-preserved platform margin section of a Late Archean–age (*ca.* 2.6–2.52 Ga) carbonate platform found in the Griqualand West structural subbasin on the Kaapvaal Craton, Northern Cape Province, South Africa (Fig. S1). Core materials collected during the Agouron Scientific Drilling Project sample deep subtidal, slope, and basinal environments on the paleogeographic upper slope. In these environments, dolomite and limestone beds interfinger with shale and banded iron formation in a predictable sequence-stratigraphic fashion (Figs. S2 and S3; refs. 30 and 31). The primary targets of our study were shale-rich lithologies developed at sea level lowstand (31) with high organic carbon (32) and reactive iron loadings (33) that accumulated significant amounts of pyrite during early diagenesis—a pattern widely observed across the platform margin (Fig. S4; refs. 30, 32, and 34) and expected for the organic diagenesis of iron-rich sediments (35). These rocks provide a compelling opportunity to study the dynamics of the Archean sulfur cycle in a marine sedimentary basin that accumulated iron formation throughout its history (30, 36, 37).

Despite the high overall quality of preservation of these geological materials, petrographic textures (Fig. S5) indicate that the macroscopic sulfide-bearing phases display origins ranging from precipitation during early diagenesis (e.g., nodules with differential compaction, intraclast breccias, and soft sediment deformation) to late diagenesis and metamorphism (nodules without differential compaction, overgrowth rims and cements on early diagenetic chert nodules, millimeter-scale euhedral pyrites, and cross-cutting veins). In addition, the samples also contain abundant submillimeter finely disseminated sulfide-bearing minerals. Previous study of these materials by millimeter-scale sampling and bulk powders by gas-source mass spectrometry revealed variable $\delta^{34}S$ values with an average close to 0‰ but strong and variable MAF values with $\Delta^{33}S$ values, both positive and negative depending on petrographic texture (38, 39). Prior SIMS work on this succession also revealed substantial textural variation of $\Delta^{33}S$ values, and a larger range of $\delta^{34}S$ values (13, 29). These observations highlight a complex and protracted history of sulfur mineralization in this succession and the need for screening protocols to understand texture-specific analyses of multiple sulfur-isotope ratios.

Rock magnetics and paleomagnetism lend sensitive tools to query the chemical taphonomy of iron-bearing minerals and evaluate the quality of redox proxies derived from their abundance and isotopic ratios. Accordingly, core GKF01 was drilled at a 15° angle and geospatially oriented for paleomagnetic study. De Kock et al. (40) conducted an intensive paleomagnetic survey of both outcrop and drill core samples of Transvaal strata from the Griqualand West region as a part of the Agouron Drilling Project. All samples examined contain a very well developed and pervasive chemical remanence—referred to by its declination and inclination as north down—carried by ferromagnetic sulfide-bearing phases (i.e., pyrrhotite, $Fe_{(1-x)}S$ where x = 0–0.2); this overprint is tied to extensive epigenetic Pb–Zn mineralization of Transvaal strata by craton-scale Mississippi Valley-type fluids driven by the emplacement of the *ca.* 2-Ga Bushveld Complex large igneous province (Fig. S1; refs. 40 and 41). Despite the ubiquity of this magnetic component even in strata from Griqualand West, the impact of this alteration on observed isotopic signals has remained unclear.

The presence of this late, metasomatic magnetic component is especially useful because it highlights geologic samples that otherwise appear well preserved, but nonetheless contain detectable sulfide-bearing mineral phases tied to later metasomatism. We used scanning high-resolution magnetic microscopy, using superconducting quantum interference device (SQUID) sensors to image the magnetization in room-temperature samples containing diverse sulfide mineral components at a 50-μm scale (*Methods*). The sensitivity and spatial resolution offered by this technique allow the opportunity to study how these rocks have preserved biogeochemical information through a complex 2.5-billion-year history. With insight from the SQUID images, we then measured $^{33}S/^{32}S$ and $^{34}S/^{32}S$ using SIMS to make regularly spaced spot measurements in analytical grids at a similar scale (spot size ~25 μm; ref. 42). The combination of these two techniques, scanning SQUID magnetic microscopy and SIMS analytical grids, make it possible to interrogate the processes responsible for the origin and preservation of sulfur-isotopic signals in the Archean sedimentary record.

Results and Discussion

Sample domains affected by late-stage (2.05 Ga) sulfide mineralization are highlighted in the scanning SQUID images (Figs. 1*C*, 2 *B* and *E*, and 3*B*), by the presence of secondary ferromagnetic minerals of the pyrrhotite series. In general, early diagenetic pyrite nodules do not carry a remanent magnetization, but several nodules clearly contain magnetic domains (Fig. 1*C*).

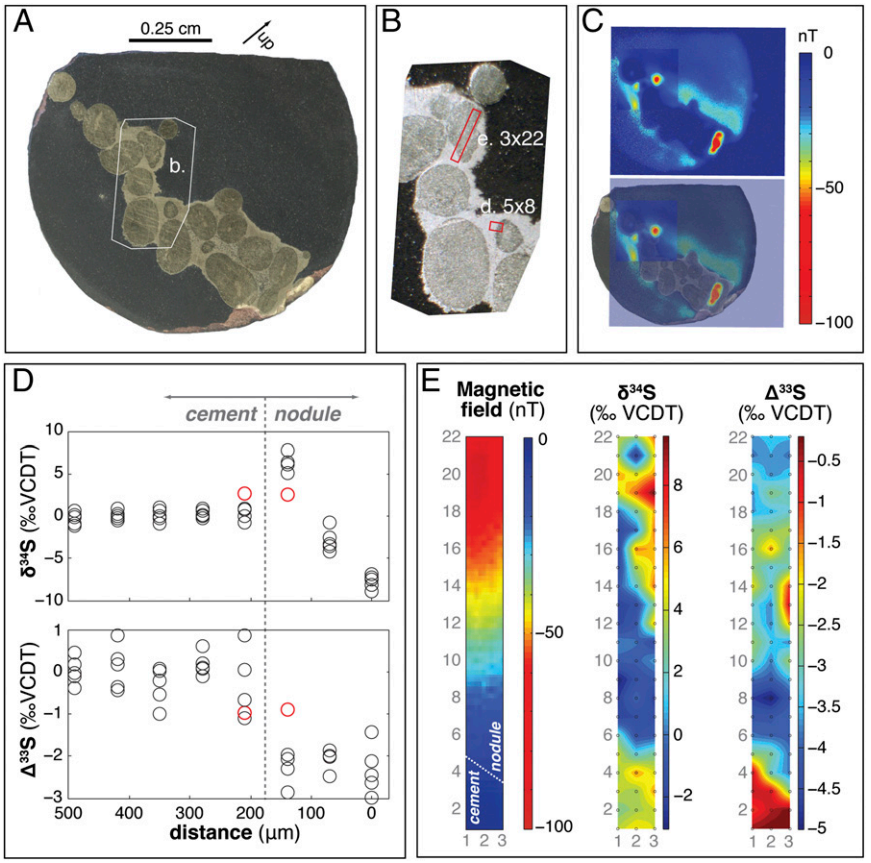

Fig. 1. Combining petrography with scanning SQUID microscopy and SIMS multiple S-isotope ratio data shows how compositions were acquired and then altered by postdepositional processes. (*A*) Reflected light photomicrograph of black shale sample (264.05 m) containing several visible phases of sulfide-bearing minerals: early diagenetic nodules, later overgrowth cement, and finely disseminated crystals in the matrix. (*B*) Reflected light photomicrograph of region outlined in *A*. Note the locations of analytical grids for sulfur-isotope data shown in *D* and *E*. Analytical grids link together individual analyses spaced at regular distances to identify isotopic trends on a length scale greater than several millimeters using SIMS. (*C*) Two scanning SQUID microscope magnetic images of the sample alone (*Upper*) and petrographic overlay (*Lower*). This image contains pixel-scale noise due to an RF interference, the source of which was eliminated before subsequent analyses. Negative values (red) show magnetic field strength into the page. Note that the magnetism is tied to finely disseminated phases in the shale matrix. In general, nodules do not contain 2.05-Ga magnetic sulfur phases, but two distinct anomalies are visible. (*D*) Multiple sulfur-isotope data from a 5×8 analytical grid crossing the contact between a nonmagnetic nodule and overgrowth cement. Unfilled data circles are larger than the measurement uncertainty ($\delta^{34}S = 0.4‰$, $\delta^{33}S = 0.3‰$, $\Delta^{33}S = 0.15‰$ 1σ). Red circles mark spot location on the contact of nodule and cement and thereby record a mixing of the different isotopic compositions. Note the distinct minor isotopic composition of the nodule from the later overgrowth and the systematic ^{34}S-enrichment of the nodule toward its margin. (*E*) Multiple sulfur-isotope ratio images constructed by linear interpolation of a 3×22 analytical grid shown alongside the magnetic image. Analysis points are shown. This grid captures a nodule with a magnetic anomaly and overgrowth cement. The variation in isotopic composition is captured by the petrographic and magnetic textures, revealing the impact of postdepositional fluids (Fig. S7).

This is in contrast to finely disseminated sulfide mineral phases in the shale matrix, which are commonly magnetic (Fig. 1*C*). This is useful because the relationships revealed by SQUID microscopy are not readily determined by petrography alone. In particular, although finely disseminated sulfide mineral phases are often preferred for sulfur-isotope analysis, the scanning SQUID data suggests that, at least in this succession, they appear most impacted by the late mineralization and may not yield primary signals. This may reflect their greater surface area and higher reactivity with metamorphic fluids; and if this is true more broadly, a different sampling strategy may be required to derive higher quality proxy data from Precambrian successions.

Multiple sulfur-isotope ratios vary between textures, within textures, and with millimeter-scale changes in rock magnetics—and these relationships document isotopic history of sulfur mineralization. For example, sample 264.05 m contains at least four S-bearing phases: early diagenetic pyrite nodules, overgrowth cement, and magnetic domains within the nodules, as well as magnetic finely disseminated crystals in the shale matrix. SIMS data shows a sharp contrast in isotope ratios (resolved by our grids to within 60 μm) at the contact between nonmagnetic nodules and the overgrowth cement (Fig. 1*D* and Fig. S6); this is still greater than expected length scales for self-diffusion of sulfur isotopes in sulfide-bearing minerals given the thermal history of this succession (43). The nodules in this sample record negative $\Delta^{33}S$ values and systematically varying $\delta^{34}S$ values; whereas, the overgrowth cement has $\Delta^{33}S$ and $\delta^{34}S$ values closer to zero per mil. These observations demonstrate that the sediments acquired their MAF before burial diagenesis and rule out a class of hypotheses positing a high-temperature burial origin for the isotope effects (23).

Our SIMS data also reveal that sulfur-isotope ratios of the sample were altered at 2.05 Ga. Five spot measurements on magnetic finely disseminated phases in the matrix show a $\delta^{34}S$ mean and variance of −0.07‰ and $1.45‰^2$, respectively, and a $\Delta^{33}S$ mean and variance of 1.09‰ and $0.54‰^2$, respectively. These magnetic $\Delta^{33}S$ values represent a distinct isotopic composition from the other textures (Fig. S7), and demonstrate the impact of metasomatic alteration. Several nodules also show distinct magnetic anomalies; for example, an analytical grid

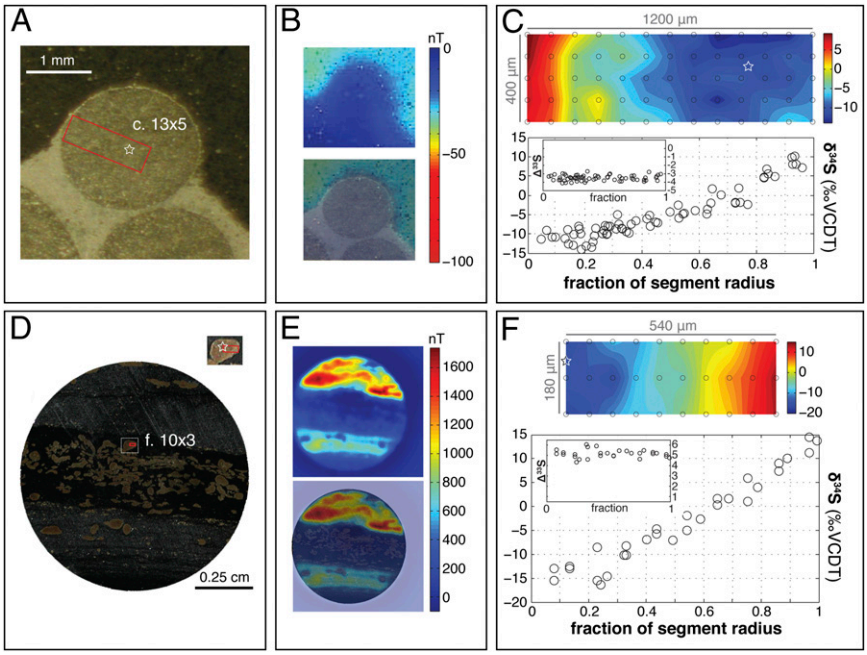

Fig. 2. Systematic $\delta^{34}S$ gradients point to substantial fractionations during sulfate reduction in these organic-rich environments. (*A*) Reflected light photomicrograph (264.05 m) of a circular nodule with overgrowth cement. Red box marks the dimensions of a 13 × 5 analytical grid shown in *C*. The white star denotes the center of a spherical segment of the nodule exposed at the surface of the sample. (*B*) Scanning SQUID microscope images of the sample alone (*Upper*) and petrographic overlay (*Lower*). This nodule does not contain late S mineralization. (*C*) Above, $\delta^{34}S$ image of the grid shown in *A*. Analysis spots are marked. (*Lower*) $\delta^{34}S$ shown as a function of spherical segment radius (center marked as a white star); $\Delta^{33}S$ data for the same segment shown (*Inset*). (*D*) Reflected light photomicrograph of a thin accumulation of black shale between two beds of detrital carbonate (1,419.40 m). Pyrite preferentially accumulated in the shale. *Inset* shows a close-up image of the nodule and 10 × 3 analytical grid shown in *F*. (*E*) Scanning SQUID microscope images of the sample alone (*Upper*) and petrographic overlay (*Lower*). Late mineralization in this sample is preferentially tied to the detrital carbonate lithology. Positive field strength values (red) indicate magnetization out of the page. (*F, Upper*) $\delta^{34}S$ image of the grid shown in *D*. Analysis spots are shown. (*Lower*) $\delta^{34}S$ shown as a function of spherical segment radius (center marked as a white star); $\Delta^{33}S$ data for the same segment shown (*Inset*). Note in both samples, the systematic ^{34}S enrichments as a function of nodule radius.

through a triangle-shaped nodule captures a continuous trend from magnetic nodule to nonmagnetic nodule to overgrowth cement (Fig. 1*E* and Fig. S6). Sulfur isotopes are distinct between these three phases (Fig. S7), in particular the magnetic nodule is characterized by higher $\Delta^{33}S$ values than the nonmagnetic parts of the nodule and both are distinct from the overgrowth cement. The isotopic composition of the magnetic nodule (Fig. 1*E*) is also distinct from the nonmagnetic portion of the nodule and overgrowth cement (Fig. S7), but could reflect mixing of a primary nodule composition and later fluids. This protracted history of sulfur mineralization shows that the minor isotopic compositions of late phases varied and do contain MAF, but were also higher than the negative $\Delta^{33}S$ values that characterize the primary phases. In principle, pyrrhotite can form from the decomposition of pyrite and loss of sulfur or with the additional of iron at high temperatures. However, either of these scenarios would imply little to no change of multiple sulfur-isotope composition. Pyrrhotite is also commonly a primary phase that acts as an important sulfur and redox buffer during metamorphism (44). The 2.05-Ga alteration event on the Kaapvaal Craton is widely reflected by epigenetic ore mineralization and the metals were transported and precipitated in sulfide-bearing

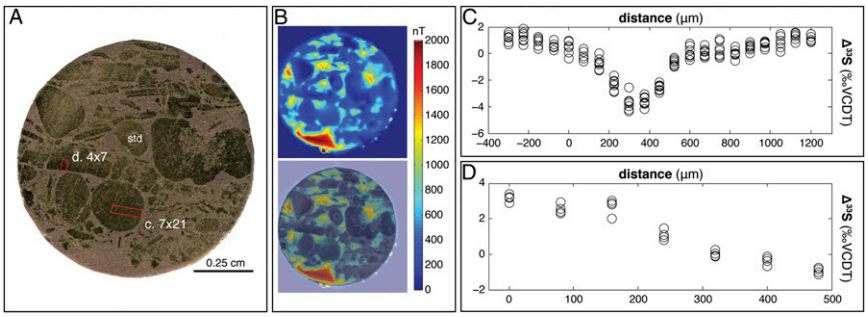

Fig. 3. Systematic $\Delta^{33}S$ gradients document a fluid with an evolving minor isotope composition. (*A*) Reflected light photomicrograph of an intraformational breccia of pyrite nodules from shallower sediments transported by mass flow downslope (290.28 m). Red boxes mark the limits of analytical grids shown in *C* and *D*. Std marks the location of an analytical standard. (*B*) Scanning SQUID microscope images of the sample alone (*Upper*) and petrographic overlay (*Lower*). The analytical domains marked in red boxes in *A* lack late S mineralization. (*C*) $\Delta^{33}S$ data of the 7 × 21 point grid in *A* as a function of distance within a single nodule reveals large, repeatable 4–5‰ gradients. (*D*) $\Delta^{33}S$ data of the 4 × 7 point grid in *A* as a function of distance within a single tabular intraclast reveals gradients that extend to either side of zero per mil.

minerals from low temperature fluids (41). The isotopic composition of late phases could record intraformational or intrabasinal redistribution of sulfur and need not require the introduction of new sulfur from fluid earth reservoirs (e.g., Paleoproterozoic seawater sulfate). This highlights a style of isotopic mixing due to late fluid flow processes that will tend to alter the MAF signal originally held by these sediments, as these processes are expected to be (largely) mass dependent.

This ability to identify and target nodules unaffected by late diagenetic and metasomatic processes provides fresh insights into biotic and abiotic sulfur-cycle processes, as they offer samples of pore fluid evolution with time. Several of these primary nodules show remarkable isotopic gradients as a function of their spherical segment radius, from negative $\delta^{34}S$ values near the center to positive $\delta^{34}S$ values near the rim (Figs. 1*D* and 2); whereas, $\Delta^{33}S$ values do not vary systematically over the same length scale (Fig. S8). This pattern implies significant sulfur-isotope fractionations (*ca.* 10–20‰, to produce the range in values observed in Figs. 1*D* and 2) occurred during DSR in these organic-rich shallow sedimentary paleoenvironments during growth of early diagenetic pyrite nodules. These data strongly support hypotheses that DSR was an important respiratory metabolism on early Earth (11–13, 16). Deep seawater in this marine basin was iron rich throughout its history (30), but even so, these $\delta^{34}S$ fractionations illustrate that sulfur metabolisms were operating in environments with insufficient ferric iron to respire the organic matter present. These fractionations are larger than anticipated and imply that either sulfate concentrations in Archean seawater were greater than ~200 μM (15) or DSR fractionations are more physiologically plastic and/or poorly predicted by sulfate concentration alone. These observations demonstrate biological participation in the Archean sulfur cycle; however, despite the large systematic fractionations revealed by the SIMS data, on average and in bulk, these rocks have $\delta^{34}S$ values near zero per mil (38, 39). From a mass-balance perspective, this suggests at least partially closed system behavior—most sulfate entering organic-rich marine sediments was converted to pyrite. This contrasts with sulfur cycling in marine sediments today wherein reoxidation of sulfide is important, and suggests that pyrite precipitation in Archean sediments was limited by sulfide rather than reactive iron (45).

Early diagenetic pyrite nodules also document an evolving fluid with regard to minor sulfur-isotope composition (Fig. 3). Large systematic gradients in $\Delta^{33}S$ (>4‰, both positive and negative values) exist within single nodules and intraclasts—trends that, intriguingly, do not correlate strongly with $\delta^{34}S$ (Fig. S8). Further, $\Delta^{33}S$ values within these single nodules cover much of the range seen in bulk throughout the entire sedimentary succession (38). These observations imply at least partially open system isotope mass-balance behavior during the growth of these nodules and intraclasts, with the sedimentary pore fluid sampling different sulfur pools on geologically short timescales. This environmental heterogeneity of $\Delta^{33}S$ values underscores the importance of incomplete but variable mixing due to sulfur-cycle processes, including microbial metabolisms and the possibility of rapid secular changes in the processes producing MAF.

Altogether, observations from this succession document the importance of mixing processes (both biotic and abiotic) at a wide range of length and timescales, including the impacts of postdepositional mineralization. The magnitudes of these mixing processes are difficult to identify simply—in consequence, the observed microscale isotopic heterogeneity challenges the use of bulk rock $\Delta^{33}S$ data as a robust stratigraphic proxy for sulfur-cycle processes. However, by leveraging information from petrography and magnetic imaging, it is possible to untangle the complex history of sulfide mineralization and arrive at a more accurate understanding of sulfur-cycle function on Earth.

Methods

We used the scanning SQUID microscope to produce images of pyrite nodules highlighting the relative differences in magnetic field strength. The relative differences in field strength captured by the SQUID microscope images uncover otherwise cryptic magnetic domains within preserved sulfide-bearing minerals. Unlike a standard SQUID rock magnetometer that measures the net magnetic moment of a sample, a scanning SQUID microscope measures the vertical component of the magnetic field on a prepared surface of a sample as it is rastered across a stationary microfabricated sensor, producing a high-resolution map (46–49). The SQUID sensor on the Caltech microscope is held at superconducting temperatures (2.6–3.8 K) on a sapphire bobbin, thermally linked with a vibration-stabilized CryoMech PT-403 pulse-tube cryocooler, eliminating the need for liquid helium. A 25-μm–thick sapphire window separates the room-temperature sample from the SQUID sensor. The SQUID apparatus remains fixed while the sample is rastered in small steps in an *x, y* grid using a nonmagnetic scanning stage; 50-μm steps were used in this study, with a resolution somewhat coarser than our SIMS spots. We collected oriented cylindrical 2.5-cm samples from the core (referenced using a ballmark system and wireline geophysical tools) using a drill press with a nonmagnetic bit. The cylindrical core was subsampled and stepwise hybrid demagnetization techniques (50) were applied to splits to confirm the presence of the north-down component magnetization vector (40). The samples were subsequently given a known isothermal remanent magnetization (IRM) of ~300 mT perpendicular to the sample surface, either into, or out of, the page. The IRM was subsequently imaged using the scanning SQUID microscope to produce a magnetic map. A wire scan (a known current flowing through a thin, linear wire film) was run in between samples as a standard to monitor sensitivity, mainly as a measure of distance from the room-temperature sample to the superconducting sensor. Because of small differences in the height of the SQUID sensor to the sample surface from sample to sample, and because the strength of the field decays as $1/r^3$, the absolute values of field strength measurements are difficult to compare between samples; however relative values within one scan can be used to precisely distinguish regions of differing magnetic properties within a sample. After obtaining SQUID images, samples were sputter coated with 30 nm of Au for SIMS analysis.

For multiple sulfur isotope analyses, we used a Cameca 7f-GEO ion microprobe housed within the Center for Microanalysis in the Division of Geological and Planetary Sciences at California Institute of Technology. We used a focused primary Cs^+ ion beam of ~4 nA rastered over an analysis area for a final spot size of ~25 × 25 μm. This configuration makes the 7f-GEO ideally suited for identifying isotope ratio trends within and between different textures revealed by petrography and scanning SQUID microscopy using closely and regularly spaced spot analyses (42, 51), although the small size of the disseminated pyrites present in many samples precludes reliable analysis of all but the larger grains that make up this texture. A primary objective in SIMS analysis is operating at sufficient mass-resolving power (MRP) to separate ions of similar mass, but also allowing enough transmission of secondary ions to make precise measurements. When measuring multiple sulfur isotopes (^{32}S, ^{33}S, ^{34}S), the minimum MRP is ~3,900 to separate ^{33}S from the ^{32}SH ion. Operating with these analytical conditions, we typically achieve ~10^9 counts per second of ^{32}S, and ~10^8 and ~10^7 counts per second for ^{34}S and ^{33}S, respectively. We used regularly spaced analytical grids of spot analyses collected incrementally from end to end (back and forth) to identify isotopic trends on a length scale greater than a millimeter. Analyses of sample unknowns were bracketed by measurements of standards every 10–15 measurements. We used a Caltech internal pyrite standard—grains of igneous pyrite from Peru (Orocampa district)—for which the multiple sulfur-isotopic composition was determined by gas source mass spectrometry of SF_6 (as in ref. 52; $\delta^{34}S$ 1.024‰ $\delta^{33}S$ 0.608‰, Vienna Canyon Diablo Troilite). Our standards were embedded within the samples close to the desired analytical region, and polished to obtain a flat surface (either as a thin section or thick section). This provides similar beam conditions for measurements of both standards and sample unknowns, a widely recognized challenge that must be met to produce accurate data (53). The isotope ratio data were corrected for Faraday cup yield differences and instrumental mass fractionation (Dataset S1). External precision, defined as the SD of multiple adjacent measurements of standards, is typically better than $\delta^{34}S$ = 0.4‰, $\delta^{33}S$ = 0.3‰, $\Delta^{33}S$ = 0.15‰ (1σ).

ACKNOWLEDGMENTS. This paper benefited greatly from the thoughtful comments of two anonymous reviewers. The Agouron Institute and National Aeronautic and Space Administration Exobiology Award NNX09AM91G supported this work.

1. Farquhar J, Bao H, Thiemens M (2000) Atmospheric influence of Earth's earliest sulfur cycle. *Science* 289(5480):756–759.
2. Bekker A, et al. (2004) Dating the rise of atmospheric oxygen. *Nature* 427(6970): 117–120.
3. Guo Q, et al. (2009) Reconstructing Earth's surface oxidation across the Archean-Proterozoic transition. *Geology* 37:399–402.
4. Farquhar J, Savarino J, Airieau S, Thiemens MH (2001) Observation of wavelength-sensitive mass-independent sulfur isotope effects during SO2 photolysis: Implications for the early atmosphere. *J Geophys Res* 106:32829–32839.
5. Lyons JR (2009) Atmospherically-derived mass-independent sulfur isotope signatures, and incorporation into sediments. *Chem Geol* 267:164–174.
6. Pavlov AA, Kasting JF (2002) Mass-independent fractionation of sulfur isotopes in Archean sediments: Strong evidence for an anoxic Archean atmosphere. *Astrobiology* 2(1):27–41.
7. Gaillard F, Scaillet B, Arndt NT (2011) Atmospheric oxygenation caused by a change in volcanic degassing pressure. *Nature* 478(7368):229–232.
8. Halevy I, Johnston DT, Schrag DP (2010) Explaining the structure of the Archean mass-independent sulfur isotope record. *Science* 329(5988):204–207.
9. Meyer B, Kuever J (2007) Phylogeny of the alpha and beta subunits of the dissimilatory adenosine-5-phosphosulfate (APS) reductase from sulfate-reducing prokaryotes–Origin and evolution of the dissimilatory sulfate-reduction pathway. *Microbiology* 153(Part 7): 2026–2044.
10. Xiong J, Fischer WM, Inoue K, Nakahara M, Bauer CE (2000) Molecular evidence for the early evolution of photosynthesis. *Science* 289(5485):1724–1730.
11. Ueno Y, Ono S, Rumble D, Maruyama S (2008) Quadruple sulfur isotope analysis of ca. 3.5 Ga Dresser Formation: New evidence for microbial sulfate reduction in the early Archean. *Geochim Cosmochim Acta* 72:5675–5691.
12. Shen Y, Farquhar J, Masterson A, Kaufman AJ, Buick R (2009) Evaluating the role of microbial sulfate reduction in the early Archean using quadruple isotope systematics. *Earth Planet Sci Lett* 279:383–391.
13. Kamber BS, Whitehouse MJ (2007) Micro-scale sulphur isotope evidence for sulphur cycling in the late Archean shallow ocean. *Geobiology* 5:5–17.
14. Strauss H (2003) Sulphur isotopes and the early Archaean sulphur cycle. *Precambrian Res* 126:349–361.
15. Habicht KS, Gade M, Thamdrup B, Berg P, Canfield DE (2002) Calibration of sulfate levels in the Archean ocean. *Science* 298(5602):2372–2374.
16. Ohmoto H, Kakegawa T, Lowe DR (1993) 3.4-billion-year-old biogenic pyrites from Barberton, South Africa: Sulfur isotope evidence. *Science* 262:555–557.
17. Towe KM (2000) The Archean atmosphere and sedimentary sulfides. *Science* 289(5483):1297–1298.
18. Philippot P, et al. (2007) Early Archaean microorganisms preferred elemental sulfur, not sulfate. *Science* 317(5844):1534–1537.
19. Roerdink DL, Mason PRD, Farquhar J, Reimer T (2012) Multiple sulfur isotopes in Paleoarchean barites identify an important role for microbial sulfate reduction in the early marine environment. *Earth Planet Sci Lett* 331–332:177–186.
20. Eriksson KA, Simpson EL, Master S, Henry G (2005) Neoarchaean (c. 2.58 Ga) halite casts: Implications for palaeoceanic chemistry. *J Geol Soc London* 162:789–799.
21. Grotzinger JP, Kasting JF (1993) New constraints on Precambrian ocean composition. *J Geol* 101(2):235–243.
22. Schröder S, Bekker A, Beukes NJ, Strauss H, Van Niekerk HS (2008) Rise in seawater sulphate concentration associated with the Paleoproterozoic positive carbon isotope excursion: Evidence from sulphate evaporites in the ~2.2–2.1 Gyr shallow-marine Lucknow Formation, South Africa. *Terra Nova* 20:108–117.
23. Watanabe Y, Farquhar J, Ohmoto H (2009) Anomalous fractionations of sulfur isotopes during thermochemical sulfate reduction. *Science* 324(5925):370–373.
24. Lasaga AC, Otake T, Watanabe Y, Ohmoto H (2008) Anomalous fractionation of sulfur isotopes during heterogeneous reactions. *Earth Planet Sci Lett* 268:225–238.
25. Oduro H, et al. (2011) Evidence of magnetic isotope effects during thermochemical sulfate reduction. *Proc Natl Acad Sci USA* 108(43):17635–17638.
26. Pufahl PK, Hiatt EE (2012) Oxygenation of the Earth's atmosphere–ocean system: A review of physical and chemical sedimentologic responses. *Mar Pet Geol* 32:1–20.
27. Williford KH, Van Kranendonk MJ, Ushikubo T, Kozdon R, Valley JW (2011) Constraining atmospheric oxygen and seawater sulfate concentrations during Paleoproterozoic glaciation: In situ sulfur three-isotope microanalysis of pyrite from the Turee Creek Group, Western Australia. *Geochim Cosmochim Acta* 75:5686–5705.
28. Johnson JE, et al. (2013) Manganese-oxidizing photosynthesis before the rise of cyanobacteria. *Proc Natl Acad Sci USA* 110(28):11238–11243.
29. Farquhar J, et al. (2013) Pathways for Neoarchean pyrite formation constrained by mass-independent sulfur isotopes. *Proc Natl Acad Sci USA* 110(44):17638–17643.
30. Fischer WW, Knoll AH (2009) An iron shuttle for deepwater silica in Late Archean and Early Paleoproterozoic iron formation. *Geol Soc Am Bull* 121:222–235.
31. Sumner DY, Beukes NJ (2006) Sequence stratigraphic development of the Neoarchean Transvaal carbonate platform, Kaapvaal Craton, South Africa. *South African Journal of Geology* 109:11–22.
32. Fischer WW, et al. (2009) Isotopic constraints on the Late Archean carbon cycle from the Transvaal Supergroup along the western margin of the Kaapvaal Craton, South Africa. *Precambrian Res* 169:15–27.
33. Kendall B, et al. (2010) Pervasive oxygenation along late Archaean ocean margins. *Nat Geosci* 3:647–652.
34. Beukes NJ, Klein C, Kaufman AJ, Hayes JM (1990) Carbonate petrography, kerogen distribution, and carbon and oxygen isotope variations in an early Proterozoic transition from limestone to iron-formation deposition, Transvaal Supergroup, South Africa. *Econ Geol* 85(4):663–690.
35. Walker JCG (1984) Suboxic diagenesis in banded iron formations. *Nature* 309:340–342.
36. Beukes NJ (1987) Facies relations, depositional environments and diagenesis in a major early Proterozoic stromatolitic carbonate platform to basinal sequence, Campbellrand Subgroup, Transvaal Supergroup, Southern Africa. *Sediment Geol* 54:1–46.
37. Beukes N, Klein C (1992) Models for iron-formation deposition. *The Proterozoic Biosphere: A Multidisciplinary Study*, eds Schopf JW, Klein C (Cambridge Univ Press, Cambridge, UK).
38. Ono S, Beukes NJ, Rumble D (2009) Origin of two distinct multiple-sulfur isotope compositions of pyrite in the 2.5 Ga Klein Naute Formation, Griqualand West Basin, South Africa. *Precambrian Res* 169:48–57.
39. Ono S, Kaufman AJ, Farquhar J, Sumner DY, Beukes NJ (2009) Lithofacies control on multiple-sulfur isotope records and Neoarchean sulfur cycles. *Precambrian Res* 169: 58–67.
40. De Kock MO, et al. (2009) Paleomagnetism of a Neoarchean-Paleoproterozoic carbonate ramp and carbonate platform succession (Transvaal Supergroup) from surface outcrop and drill core, Griqualand West region, South Africa. *Precambrian Res* 169: 80–99.
41. Gleason JD, Gutzmer J, Kesler SE, Zwingmann H (2011) 2.05-Ga isotopic ages for transvaal Mississippi Valley-type deposits: Evidence for large-scale hydrothermal circulation around the Bushveld Igneous Complex. *S Afr J Geol* 119:69–80.
42. Fike DA, et al. (2009) The effect of sulfate concentration on (sub)millimeter-scale sulfide δ34S in hypersaline cyanobacterial mats over the diurnal cycle. *Geochim Cosmochim Acta* 73:6187–6204.
43. Watson EB, Cherniak DJ, Frank EA (2009) Retention of biosignatures and mass-independent fractionations in pyrite: Self-diffusion of sulfur. *Geochim Cosmochim Acta* 73:4792–4802.
44. Craig JR (1993) The metamorphism of pyrite and pyritic ores: An overview. *Mineral Mag* 57:3–18.
45. Raiswell R (2011) Iron transport from the continents to the open ocean: The aging–rejuvenation cycle. *ELEMENTS* 7:101–106.
46. Weiss BP, et al. (2000) A low temperature transfer of ALH84001 from Mars to Earth. *Science* 290(5492):791–795.
47. Weiss BP, Lima EA, Fong LE, Baudenbacher FJ (2007) Paleomagnetic analysis using SQUID microscopy. *J Geophys Res* 112:B09105.
48. Bailey JV, et al. (2010) Pseudofossils in relict methane seep carbonates resemble endemic microbial consortia. *Palaeogeogr Palaeoclimatol Palaeoecol* 285:131–142.
49. Baudenbacher F, Peters NT, Wikswo JP (2002) High resolution low-temperature superconductivity superconducting quantum interference device microscope for imaging magnetic fields of samples at room temperatures. *Rev Sci Instrum* 73:1247–1254.
50. Kirschvink JL, Kopp RE, Raub TD, Baumgartner CT, Holt JW (2008) Rapid, precise, and high-sensitivity acquisition of paleomagnetic and rock-magnetic data: Development of a low-noise automatic sample changing system for superconducting rock magnetometers. *Geochem Geophys Geosyst* 9:Q05Y01. Available at http://authors.library.caltech.edu/10392/.
51. Fike DA, Gammon CL, Ziebis W, Orphan VJ (2008) Micron-scale mapping of sulfur cycling across the oxycline of a cyanobacterial mat: A paired nanoSIMS and CARD-FISH approach. *ISME J* 2(7):749–759.
52. Ono S, Wing B, Rumble D, Farquhar J (2006) High precision analysis of all four stable isotopes of sulfur (32S, 33S, 34S and 36S) at nanomole levels using a laser fluorination isotope-ratio-monitoring gas chromatography–mass spectrometry. *Chem Geol* 225:30–39.
53. Valley JW, Kita NT (2009) In situ oxygen isotope geochemistry by ion microprobe. *MAC Short Course: Secondary Ion Mass Spectrometry in the Earth Sciences*, ed Fayek M (Mineralogical Association of Canada, Toronto), Vol 41, pp 19–63.